nature communications

Article

https://doi.org/10.1038/s41467-025-61939-z

Structure of human mitochondrial pyruvate carrier MPC1 and MPC2 complex

Received: 27 January 2025

Accepted: 3 July 2025

Published online: 21 July 2025

Check for updates

Yingyuan Sun[1,6], Yaru Wang[2,6], Zheng Xing[3,4,6], Dongyu Li[1], Rong Wang[1], Baozhi Chen[2], Ning Zhou[2], Alyssa Ayala[2], Benjamin P. Tu[3,4] & Xiaofeng Qi[2,5]

The Mitochondrial Pyruvate Carrier (MPC) bridges cytosolic and mitochondrial metabolism by transporting pyruvate into mitochondria for ATP production and biosynthesis of various essential molecules. MPC functions as a heterodimer composed of MPC1 and MPC2 in most mammalian cells. Here, we present the cryogenic electron microscopy (cryo-EM) structures of the human MPC1-2 complex in the mitochondrial intermembrane space (IMS)-open state and the inhibitor-bound in the mitochondrial matrix-open state. Structural analysis shows that the transport channel of MPC is formed by the interaction of transmembrane helix (TM) 1 and TM2 of MPC1 with TM2 and TM1 of MPC2, respectively. UK5099, a potent MPC inhibitor, shares the same binding site with pyruvate at the matrix side of the transport channel, stabilizing MPC in its matrix-open conformation. Notably, a functional W82F mutation in MPC2 leads to the complex in an IMS-open conformation. Structural comparisons across different conformations, combined with yeast rescue assays, reveal the mechanisms of substrate binding and asymmetric conformational changes in MPC during pyruvate transport across the inner mitochondrial membrane (IMM) as well as the inhibitory mechanisms of MPC inhibitors.

Pyruvate plays a pivotal role in cellular metabolism by linking cytoplasmic and mitochondrial processes. Generated from glucose and lactate, pyruvate is transported into the mitochondria for further oxidation under aerobic conditions[1]. Inside the mitochondrial matrix, pyruvate dehydrogenase (PDH) decarboxylates pyruvate to form acetyl-CoA, which then enters the tricarboxylic acid (TCA) cycle for oxidation and ATP production via oxidative phosphorylation (OXPHOS)[2]. Alternatively, pyruvate can be carboxylated by pyruvate carboxylase (PC) to produce oxaloacetate, which supports biosynthetic processes including nucleotide and amino acid synthesis, de novo lipogenesis, and gluconeogenesis[3] (Fig. 1a).

The relocation of pyruvate into mitochondria is a gating event in its metabolism. Due to the impermeability of the inner mitochondrial membrane (IMM), pyruvate requires a specific transporter, the Mitochondrial Pyruvate Carrier (MPC), to enter the mitochondrial matrix[4] (Fig. 1a). In yeast, MPC is encoded by three homologous genes (*MPC1*, *MPC2*, and *MPC3*), forming either an MPC1-2 heterodimer under fermentative conditions (MPC_{FERM}) or an MPC1-3 heterodimer under respiratory conditions (MPC_{OX}) for pyruvate transport[5–8]. In mammals, three homologous genes of MPC (*MPC1*, *MPC1-like* (*MPC1L*), and *MPC2*) have been identified. Pyruvate transport is mediated by the MPC1-2 heterodimer in most mammalian cells, while the MPC1L-2 heterodimer is specific to spermatocytes[6,7,9]. Both MPC1 and MPC2 are small IMM proteins (109 and 127 amino acids for human MPC1 and MPC2, respectively) and each contains an amphipathic helix at the N-terminus. Using a thiol-reactive dye that selectively labels cysteine

[1]Department of Molecular Genetics, University of Texas Southwestern Medical Center, Dallas, TX, USA. [2]Department of Molecular Biology, University of Texas Southwestern Medical Center, Dallas, TX, USA. [3]Department of Biochemistry, University of Texas Southwestern Medical Center, Dallas, TX, USA. [4]Howard Hughes Medical Institute, University of Texas Southwestern Medical Center, Dallas, TX, USA. [5]Harold C. Simmons Comprehensive Cancer Center, University of Texas Southwestern Medical Center, Dallas, TX, USA. [6]These authors contributed equally: Yingyuan Sun, Yaru Wang, Zheng Xing.
e-mail: xiaofeng.qi@utsouthwestern.edu

https://doi.org/10.1038/s41467-025-61939-z

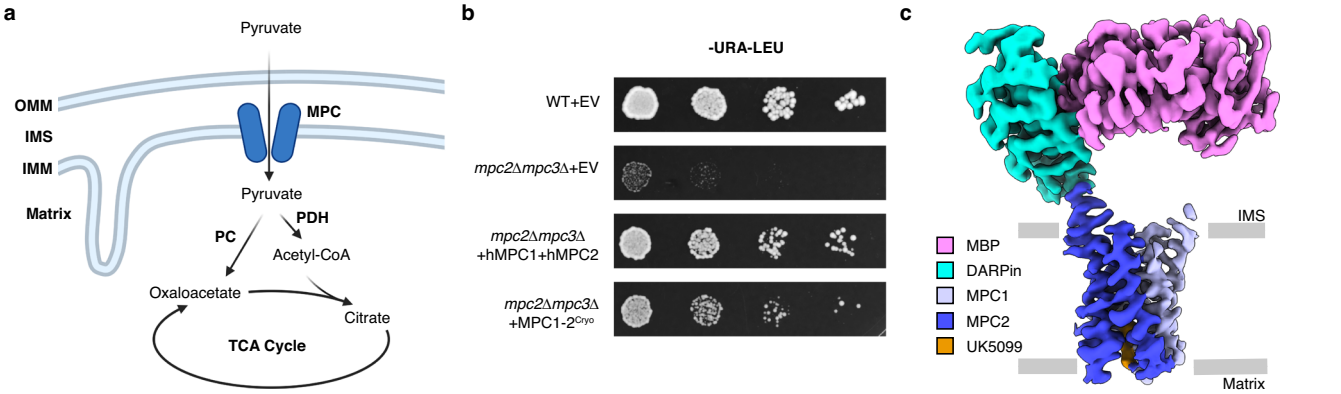

Fig. 1 | Structure determination of human MPC1-2 complex. a A brief schematic diagram of pyruvate transport and metabolism. Pyruvate is transported into the matrix by the Mitochondrial Pyruvate Carrier (MPC) and subsequently converted to acetyl-CoA by the pyruvate dehydrogenase (PDH) complex or oxaloacetate by the pyruvate carboxylase (PC). OMM outer mitochondrial membrane, IMM inner mitochondrial membrane, IMS mitochondrial intermembrane space, TCA tricarboxylic acid. Created in BioRender. Qi, X. (2025) https://BioRender.com/ahg95gr. **b** Serial dilutions of wild-type (WT) and *mpc2*Δ*mpc3*Δ yeast strains spotted on medium lacking leucine (-URA-LEU). In yeast, the de novo synthesis of leucine begins with mitochondrial pyruvate, therefore growth on plates lacking leucine is indicative of a functional MPC. The cells were transformed with empty vector (EV), wild-type human MPC1-2 or MPC1-2^{Cryo}. **c** Cryo-EM map of MPC1-2^{Cryo}–UK5099. Maltose-binding protein (MBP), designed ankyrin-repeat protein off7 (DARPin), MPC1, MPC2 and UK5099 are shown as violet, turquoise, light blue, blue and orange, respectively.

residues located in the intermembrane space (IMS) but not in the matrix, a previous study determined that the N-termini of MPC protein is located in the matrix[5]. Subsequent structural predictions indicated that MPC proteins contain three transmembrane helices[8,10,11].

Given its fundamental role in cellular metabolism, MPC proteins are associated with various human diseases related to mitochondrial dysfunction[12,13]. Many cancers have upregulated glycolysis, known as the Warburg Effect, as well as disrupted MPC proteins, which promote aerobic glycolysis, growth, metastasis, and lead to poor prognosis[3]. Additionally, disruption of MPC proteins in the liver and skeletal muscle has shown beneficial effects on type 2 diabetes (T2D), including increased glucose uptake, fat oxidation, insulin sensitivity and reduced gluconeogenesis[14–16]. Importantly, neurodegenerative diseases are associated with metabolic disorders characterized by the decrease of importing or metabolizing energy sources, which can either derive from mitochondrial dysfunction or lead to it[17]. Notably, MPC inhibitor MSDC0160, a derivative of thiazolidinediones (TZDs), has shown promising results for Parkinson's and Alzheimer's diseases (PD and AD) in animal models and clinical trials[18–20]. Although MPC hold great promise for the treatment of diseases, such as neurodegenerative disorders, cancer, and diabetes, the lack of knowledge on the structure of MPC and its transport mechanism is limiting the understanding of mitochondrial metabolism regulation and the development of drugs targeting MPC.

In this work, we determine the cryo-EM structures of the human MPC1-2 complex in multiple states. Combining the functional assays, we uncover the transport and inhibitory mechanisms of MPC.

Results

Structure determination of human MPC1-2 complex

We co-expressed the full-length human MPC1 with a C-terminal Flag tag and full-length human MPC2 with a C-terminal 6xHis tag in HEK293 GnTI$^-$ cells and purified the protein complex with anti-Flag affinity resin and size exclusion chromatography (SEC). The results showed that MPC1 and MPC2 appeared at a 1:1 molar ratio in a single peak (Supplementary Fig. 1a). Previous results indicated that MPC1 and MPC2 function as a heterodimer which is around 26 kDa, far below the typical size limitation for structure determination using cryo-EM[21]. To increase the particle size for cryo-EM study, we fused a Maltose-binding protein (MBP)-Strep II tag to the C-terminus of MPC1 (full-length) with a flexible linker. Meanwhile, a MBP binding protein, designed ankyrin-repeat protein off7 (DARPin)[22], with a C-terminal Flag tag, was added to the C-terminus of MPC2 (residues 1-124) by helical linking (Supplementary Fig. 1b). This strategy was adapted from a recent study on the structures of human Spinster 2 (SPNS2)[23] and Vesicular monoamine transporter 2 (VMAT2)[24]. AlphaFold predictions[25] indicate that the engineered MPC1 and MPC2 can form a stable complex without altering the overall structure of the wild-type MPC1-2 complex (Supplementary Fig. 1b). Next, we co-expressed and purified these two engineered proteins using the same protocol as wildtype MPC1-2. MPC1-MBP-Strep II and MPC2-DARPin-Flag form a complex at a 1:1 molar ratio (Supplementary Fig. 1c). We named this complex as MPC1-2^{Cryo}.

To validate the pyruvate transport activity of MPC1-2^{Cryo}, we made a *mpc1* knockout (*mpc1*Δ) yeast (*Saccharomyces cerevisiae*) strain and a *mpc2mpc3* double knockout (*mpc2*Δ*mpc3*Δ) yeast strain (Supplementary Fig. 2a, b). Consistent with previous results[6], the growth defects of *mpc2*Δ*mpc3*Δ yeast strain can be rescued by mammalian *mpc1* and *mpc2* together, but not mammalian *mpc2* alone (Supplementary Fig. 2b, d), whereas the growth defects of *mpc1*Δ yeast strain can be rescued by mammalian *mpc1* alone (Supplementary Fig. 2a, c)[6]. Therefore, *mpc2*Δ*mpc3*Δ strain was used for validating the activity of MPC1-2^{Cryo}. When MPC1-2^{Cryo} was overexpressed, the *mpc2*Δ*mpc3*Δ strain was rescued with slightly lower efficiency compared to overexpressing the wild-type MPC1-2 complex, demonstrating that MPC1-2^{Cryo} forms a functional complex (Fig. 1b) and the MBP-DARPin tags may restrict the conformational flexibility of MPC, thereby reducing its activity.

The MBP-DARPin complex provided sufficient structural features outside of the detergent micelle for particle alignment during the cryo-EM data processing (Supplementary Fig. 3a, b and Supplementary Table 1). However, due to the high flexibility of MPC1-2 complex, a low-resolution map was observed in the presence of pyruvate and the transmembrane helices (TMs) of MPC1 and MPC2 were partially resolved (Supplementary Fig. 3a, b). To stabilize the MPC1-2 complex, we purified MPC1-2^{Cryo} in the presence of UK5099, a potent MPC inhibitor described with others[8,26]. At 15 μM, UK5099 stabilized the complex, allowing us to determine the structure of MPC1-2^{Cryo}–UK5099 at an overall resolution of 3.12 Å and a local resolution of 3.57 Å when masking the transmembrane domain of MPC1-2 (Fig. 1c, Supplementary Fig. 4a–f and Supplementary Table 1).

Structure of MPC1-2 at matrix-open state

Previous results showed that the N-terminus of MPC1 and MPC2 reside in the mitochondrial matrix[5]. In the MPC1-2^{Cryo}–UK5099 structure, the

https://doi.org/10.1038/s41467-025-61939-z

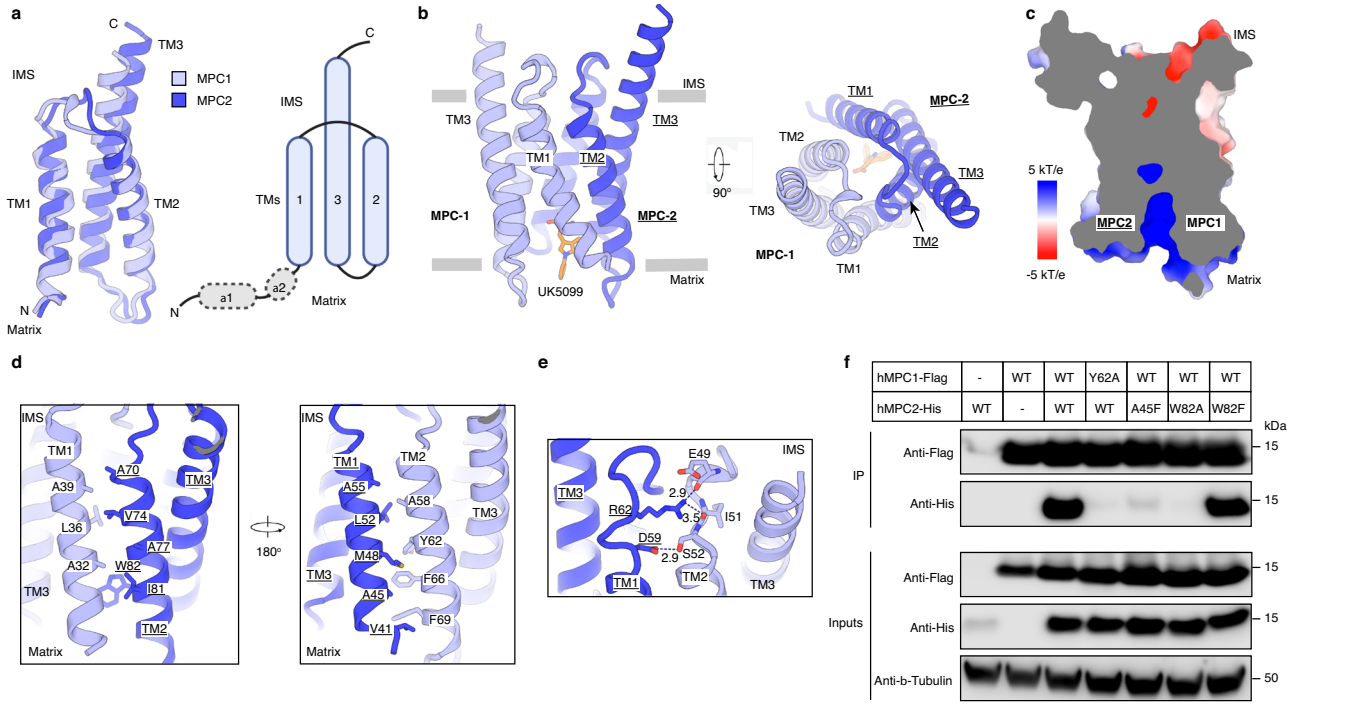

Fig. 2 | Structure of MPC1-2 in the matrix-open state. a Structural alignment of MPC1 and MPC2 from MPC1-2^{Cryo}–UK5099 structure performed using PyMOL, and the topology of MPC. MPC1 and MPC2 are shown in light blue and blue, respectively. The flexible N-terminal helices are indicated in gray. Structural diagram is created in BioRender. Qi, X. (2025) https://BioRender.com/ihdr6wh. **b** Overall structure of MPC1-2 form the IMM side view and top view. UK5099 is shown as orange sticks. **c** The electrostatic surface representation of MPC1-2 complex indicating a matrix-open state. **d** The nonpolar side chains between MPC1-TM1 and MPC2-TM2, MPC1-TM2 and MPC2-TM1 in the matrix-open state. **e** The hydrogen bonds (shown as dashed lines with distances (Å) labeled) between MPC1 and MPC2 at IMS side. **f** Co-immunoprecipitation of MPC1 and 2 complex. MPC1-Flag and MPC2-His were co-transfected to HEK293T cells and the MPC1-2 complexes were precipitated by anti-Flag M2 resin. MPC1 and MPC2 were detected by anti-Flag and anti-His antibodies. β-tubulin was used as an internal control. The experiment was repeated at least three times with similar results.

N-terminal amphipathic helices (denoted as α1 and α2, Fig. 2a) of MPC1 and MPC2 attach on the surface of the detergent micelle and are relatively flexible (Supplementary Fig. 4f). Therefore, they were not built in the structure model due to the low local resolution. The three TMs for both MPC1 and MPC2 were clearly resolved, showcasing similar topology, with the C-terminus located in the mitochondrial intermembrane space (IMS) (Fig. 2a and Supplementary Fig. 4e). The root-mean-square deviation (RMSD) of the TMs of MPC1 and MPC2 in MPC1-2^{Cryo}–UK5099 structure is 0.854 (Fig. 2a). The three TMs in both MPC1 and MPC2 follow a 1-3-2 arrangement, with TM3 positioned between TMs 1 and 2 in each protein. The TM1 of MPC1 packs against the TM2 of MPC2 while the TM2 of MPC1 interacts with the TM1 of MPC2, forming a pseudo-symmetric six-helix bundle (Fig. 2a, b).

MPC proteins belong to the recently identified family of transporters known as triple-helix-bundle (THB) transporters. These transporters use a single THB as their basic subunit and require two THBs to form a functional unit[27]. THB transporters are further categorized into two subgroups: subgroup-1 transporters contain a single THB per protomer and function as dimers, such as MPC and the bacterial SemiSWEET transporter, a homodimer that facilitates sugar transport across bacterial cell membranes[28–32] (Supplementary Fig. 5a–c); subgroup-2 transporters feature two THBs linked by a connecting TM and function as monomers (Supplementary Fig. 5d), such as eukaryotic SWEET transporters (responsible for sugar transport)[33,34] and PQ-loop transporters (responsible for amino acid transport, such as Cystinosin, a proton-driven lysosomal cystine transporter)[27] (Supplementary Fig. 5e). Interestingly, the KDEL receptor (KDELR), while not a transporter, shares a similar structure with subgroup-2 THB transporters[35] (Supplementary Fig. 5f). These structures revealed that MPC shares the same topology as THB proteins, characterized by a 1-3-2 arrangement of transmembrane helices. Previous structures have reported the SemiSWEET transporter in outward-open, occluded, and inward-open states (Supplementary Fig. 5c). The MPC1-2^{Cryo}–UK5099 structure is open on the matrix side and closed on the IMS side, indicating that it represents a matrix-open conformation of the MPC, corresponding to the outward-open state of SemiSWEET (Fig. 2c).

MPC1 and MPC2 interface

Further structural analysis showed that the interactions between MPC1-TM1 and MPC2-TM2 are mainly mediated by nonpolar residues involving Ala32, Leu36 and Ala39 of MPC1 and Ala70, Val74, Ala77, Ile81 and Trp82 of MPC2 (Fig. 2d). Similarly, Ala58, Tyr62, Phe66 and Phe69 of MPC1 and Val41, Ala45, Met48, Leu52 and Ala55 of MPC2 contribute to the interactions between MPC1-TM2 and MPC2-TM1 (Fig. 2d). Additionally, Arg62 of MPC2 interacts with Glu49 and Ile51 of MPC1, Asp59 of MPC2 interacts with Ser52 of MPC1 via hydrogen bonds at the IMS side (Fig. 2e). To further validate this interface, we performed co-immunoprecipitation assays. Our results showed that MPC1^{Y62A}, MPC2^{A45F} and MPC2^{W82A} showed decreased interactions with wildtype MPC2 or MPC1, supporting our structural observations (Fig. 2f).

UK5099 binding pocket

The α-Cyanocinnamate derivative, α-Cyano-4-hydroxycinnamate (CHC) was first identified as a specific and efficient inhibitor of pyruvate transport into mitochondria[36] (Supplementary Fig. 6a). Subsequently, another derivative, UK5099, was found to be a potent MPC inhibitor and is now considered the "gold standard" for MPC inhibition[8,37] (Supplementary Fig. 6a).

In our structure, UK5099 binds to a pocket formed by both MPC1 and MPC2 on the matrix side of the MPC1-2 heterodimer (Fig. 3a). The

https://doi.org/10.1038/s41467-025-61939-z

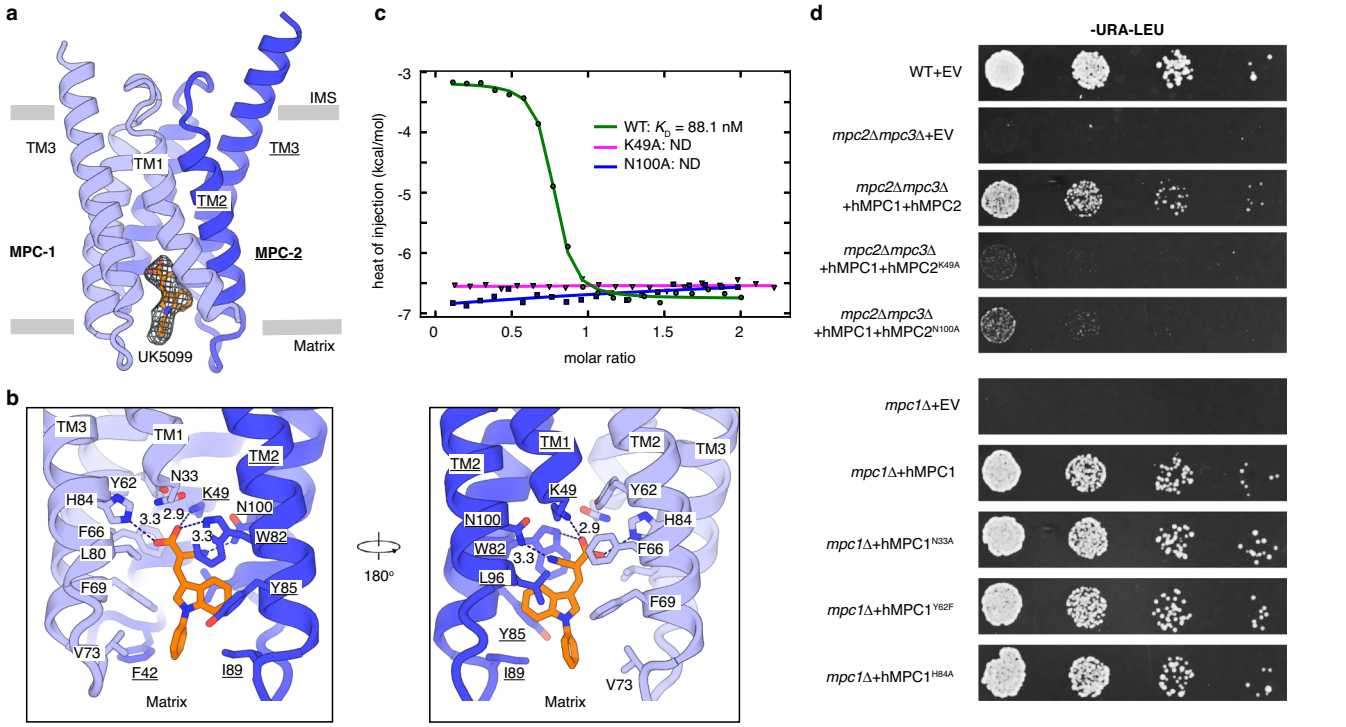

Fig. 3 | UK5099 binds to MPC1-2 complex on the matrix side. a Binding of UK5099 to MPC1-2 complex. The cryo-EM density of UK5099 is shown as green mesh isolated from the composite map of MPC1-2^{Cryo}–UK5099 in PyMOL at contour level = 10. **b** Interaction details between MPC1-2 and UK5099. The hydrogen bonds are indicated as dashed lines with distances (Å) labeled. **c** The binding affinities of UK5099 to MPC1-2 complex and its variants measured by Isothermal Titration Calorimetry (ITC). The ITC binding curves for wild-type (WT), $MPC2^{K49A}$ and $MPC2^{N100A}$ are colored in green, magenta and blue, respectively. ND not detected. **d** Serial dilutions of wild-type (WT), *mpc2*Δ*mpc3*Δ and *mpc1*Δ yeast strains spotted on medium lacking leucine (-URA-LEU). The *mpc2*Δ*mpc3*Δ cells were co-transformed with wild-type MPC1 and wild-type MPC2, $MPC2^{K49A}$ or $MPC2^{N100A}$. The *mpc1*Δ cells were transformed with wild-type MPC1, $MPC1^{N33A}$, $MPC1^{Y62F}$ or $MPC1^{H84A}$.

carboxyl group of UK5099 interacts with Lys49 of MPC2 and His84 of MPC1 through hydrophilic interactions, while the cyano group forms hydrogen bonds with Asn100 of MPC2. Additionally, considering the dynamic of the protein, Tyr62 and Asn33 of MPC1 close to UK5099 may potentially interact with the carboxyl group of UK5099 (Fig. 3b). Furthermore, hydrophobic interactions involving Phe66, Phe69, Val73, and Leu80 of MPC1, as well as Tyr85, Ile89, and Leu96 of MPC2, contribute to the binding of the indole and phenyl groups of UK5099 (Fig. 3b).

The α-Cyanocinnamate derivative inhibitors of MPC share common features, namely the carboxyl and cyano groups, which mediate the hydrophilic interactions between UK5099 and the MPC1-2 complex (Fig. 3b and Supplementary Fig. 6a). Notably, these two groups mimic the structural features of pyruvate (Supplementary Fig. 6a, b). It was previously proposed that pyruvate and all known MPC inhibitors, including α-Cyanocinnamate derivatives, TZDs, and others, contain three polar groups that may mediate hydrophilic interactions with MPC in a similar manner (Supplementary Fig. 6a–c)[8]. Supporting this hypothesis, previous data demonstrated that polar residues Lys49 and Asn100 of MPC2 are essential for the binding of both pyruvate and MPC inhibitors UK5099 and MSDC-0602K, while Asn33 and His84 of MPC1 are not critical for interacting with either pyruvate or MPC inhibitors[10].

To further investigate the binding mechanism of pyruvate and MPC inhibitors to the MPC1-2 complex, we introduced mutations in the polar residues Lys49 and Asn100 of MPC2 and employed isothermal titration calorimetry (ITC) to measure the interaction between UK5099 and MPC1-2 variants. The results revealed that the K49A and N100A mutation in MPC2 abolished binding between UK5099 and MPC1-2 (Fig. 3c). As expected, these mutations either abolished or significantly impaired the ability of ectopically expressed MPC proteins to rescue yeast growth defects (Fig. 3d and Supplementary Fig. 2d). Additionally, these mutants also significantly decreased the inhibitory ability of UK5099 to MPC1-2 complex in the yeast growth assay (Supplementary Fig. 6d). Thus, these results support our structural observations and indicate that pyruvate shares the same binding site as the polar groups of UK5099. It is also possible that mutations at Lys49 and Asn100 of MPC2 may affect the dynamics of the MPC1-2 complex during pyruvate transport and consequently alter its kinetic activity. Additionally, yeast growth rescue assays also indicated that residues Asn33, Tyr62, and His84 of MPC1 in the binding pocket are not essential for pyruvate transport (Fig. 3d and Supplementary Fig. 2c), consistent with previous studies[10].

Based on our MPC1-2^{Cryo}–UK5099 structure, we conducted a docking analysis of pyruvate molecule to MPC1-2 complex using AutoDock Vina[38] and the result showed that the carbonyl group of pyruvate formed a hydrogen bond with Lys49 of MPC2 and the carboxyl group formed hydrogen bonds with Asn100 of MPC2 (Supplementary Fig. 6e). This model is consistent with our functional analyses and might represent the binding of pyruvate to MPC in the matrix-open state.

Since UK5099 binds to the center of the MPC1-2 heterodimer and is likely to share the same binding site with pyruvate, it is tempting to hypothesize that UK5099 inhibits MPC by directly competing with pyruvate and blocking the transport channel. Furthermore, UK5099 interacts with both MPC1 and MPC2, suggesting that UK5099 may also stabilize the MPC1-2 heterodimer in the matrix-open conformation, inhibiting the potential conformational transition required for pyruvate transport. This stabilization might explain why we achieved higher resolution compared to MPC1-2^{Cryo} structure determined in the presence of pyruvate when determining the structure with UK5099. Consistently, previous thermostability shift analyses have shown that

https://doi.org/10.1038/s41467-025-61939-z

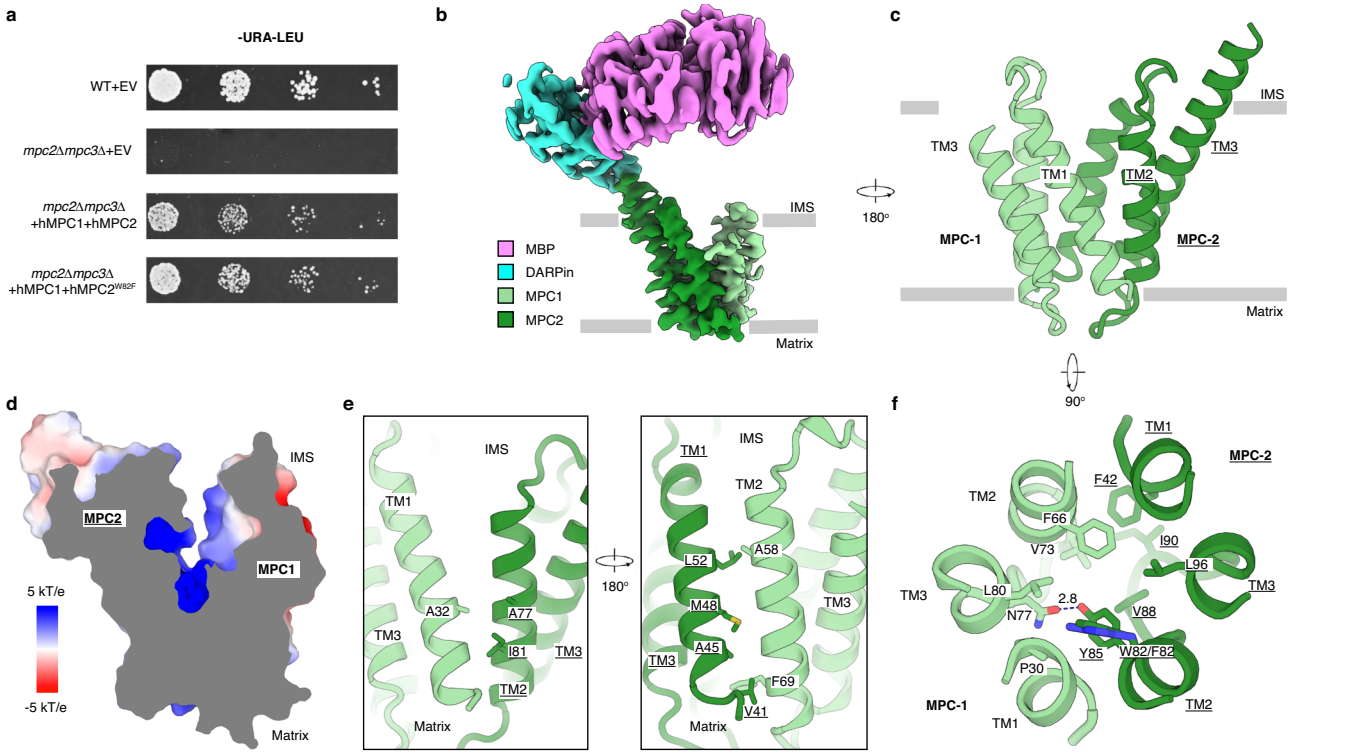

Fig. 4 | Structure of MPC1-2 in the IMS-open state. a Serial dilutions of wild-type (WT) and *mpc2Δmpc3Δ* yeast strain spotted on medium lacking leucine (-URA-LEU). The cells were co-transformed with wild-type MPC1 and wild-type MPC2 or MPC2^{W82F}. **b** Cryo-EM map of MPC1-2^{Cryo}–W82F. MBP, DARPin, MPC1 and MPC2 are shown as violet, turquoise, light green, and green, respectively. **c** Overall structure of MPC1-2^{W82F} from the IMM side view. MPC1 and MPC2 are shown as light green and green, respectively. **d** The electrostatic surface representation of MPC1-2 complex indicating a IMS-open state. **e** The nonpolar side chains between MPC1-TM1 and MPC2-TM2, MPC1-TM2 and MPC2-TM1 in the IMS-open state. **f** Interaction details between MPC1 and MPC2 within the center of the TMs on the matrix side. The hydrogen bond between MPC1-Asn77 and MPC2-Tyr85 is indicated as a dash line with distance (Å) labeled.

UK5099 can stabilize the human MPC1L-2 complex, a close analog of the MPC1-2 complex[39].

Structure of MPC1-2 at IMS-open state

The MPC is closed at the IMS side in the matrix-open conformation, suggesting the existence of other conformations that open toward the IMS, allowing pyruvate to enter the MPC from IMS of mitochondria. To capture the MPC1-2 complex in the other conformations, we introduced mutations at the MPC1 and MPC2 interface. The MPC2^{W82F} mutant was found to not affect the interaction between MPC1 and MPC2 (Fig. 2f) and presented a similar activity to the wild-type MPC2 in yeast (Fig. 4a and Supplementary Fig. 2d). We then determined the cryo-EM structure of MPC1-2^{Cryo}–W82F, resulting in an overall resolution of 2.77 Å and a local resolution of 3.31 Å when masking the transmembrane domain of MPC1-2 (Fig. 4b, c, Supplementary Fig. 7a–f and Supplementary Table 1). Similar to the D20A mutation in the *Leptospira biflexa* SemiSWEET transporter crystal structure[28], the W82F mutation in MPC2 leads to a different preferred conformation as observed in the cryo-EM reconstruction. In this structure, MPC1-2 is open towards the IMS and closed at the matrix side of mitochondria, representing an IMS-open conformation of MPC (Fig. 4d) and corresponding to the inward-open conformation of SemiSWEET (Supplementary Fig. 5c). Although the cryo-EM sample of MPC1-2^{Cryo}–W82F was prepared in the presence of pyruvate, no notable density was found to represent pyruvate in the MPC1-2^{Cryo}–W82F structure. Furthermore, comparisons of three cryo-EM maps of MPC1-2^{Cryo}, MPC1-2^{Cryo}–UK5099 and MPC1-2^{Cryo}–W82F suggest that the MPC1-2^{Cryo} structure may represent an intermediate state between the matrix-open and IMS-open states (Supplementary Figs. 4g and 7g).

Despite the conformational differences, the interactions between the TMs of MPC1 and MPC2 in the IMS-open conformation remain primarily mediated by MPC1-TM1 with MPC2-TM2, and MPC1-TM2 with MPC2-TM1 (Fig. 4e). The nonpolar residues contributing to the interactions include Ala32, Ala58, and Phe69 of MPC1, as well as Val41, Ala45, Met48, Leu52, Ala77, and Ile81 of MPC2 (Fig. 4e). Additionally, hydrophobic residues such as Pro30, Phe66, Val73, and Leu80 of MPC1, along with Phe42, Val88, Ile90, and Leu96 of MPC2, also contribute to interactions at the matrix side (Fig. 4f). The Trp82 of MPC2 locates at a hydrophobic environment at the matrix side of MPC1-2 complex (Supplementary Fig. 8a), therefore W82F mutation of MPC2 may enhance the hydrophobic interactions at IMS-open state, resulting in a preferred conformation. Interestingly, the hydrophilic interactions mediated by Asp59 and Arg62 of MPC2 at the IMS side in the matrix-open state (Fig. 2e) are disrupted due to the conformational changes in the IMS-open state. In contrast, Asn77 of MPC1 and Tyr85 of MPC2 establish a hydrogen bond at the matrix side in the IMS-open conformation (Fig. 4f).

Structures of bacterial SemiSWEET transporters at the inward-open state[28,29], human Cystinosin at the cytosol-open state[40], and rice SWEET[34] revealed that MPC shares the same topology with other THB transporters in the corresponding conformation (Supplementary Fig. 8b–d). This observation suggests that MPC may undergo a conformational transition cycle similar to other THB transporters to facilitate pyruvate transport.

Conformational changes of MPC

Structural comparisons revealed that the TM3 of MPC1 in MPC1-2^{Cryo}–W82F rotates counterclockwise by approximately 30 degrees around His84, while the TM3 of MPC2 rotates clockwise by about 6 degrees around Asn100, compared to MPC1-2^{Cryo}–UK5099 structure (Fig. 5a). Meanwhile, the distance between Gln94 in MPC1-TM3 and Gln110 in MPC2-TM3 increases from ~20 Å to ~27 Å at the matrix side,

https://doi.org/10.1038/s41467-025-61939-z

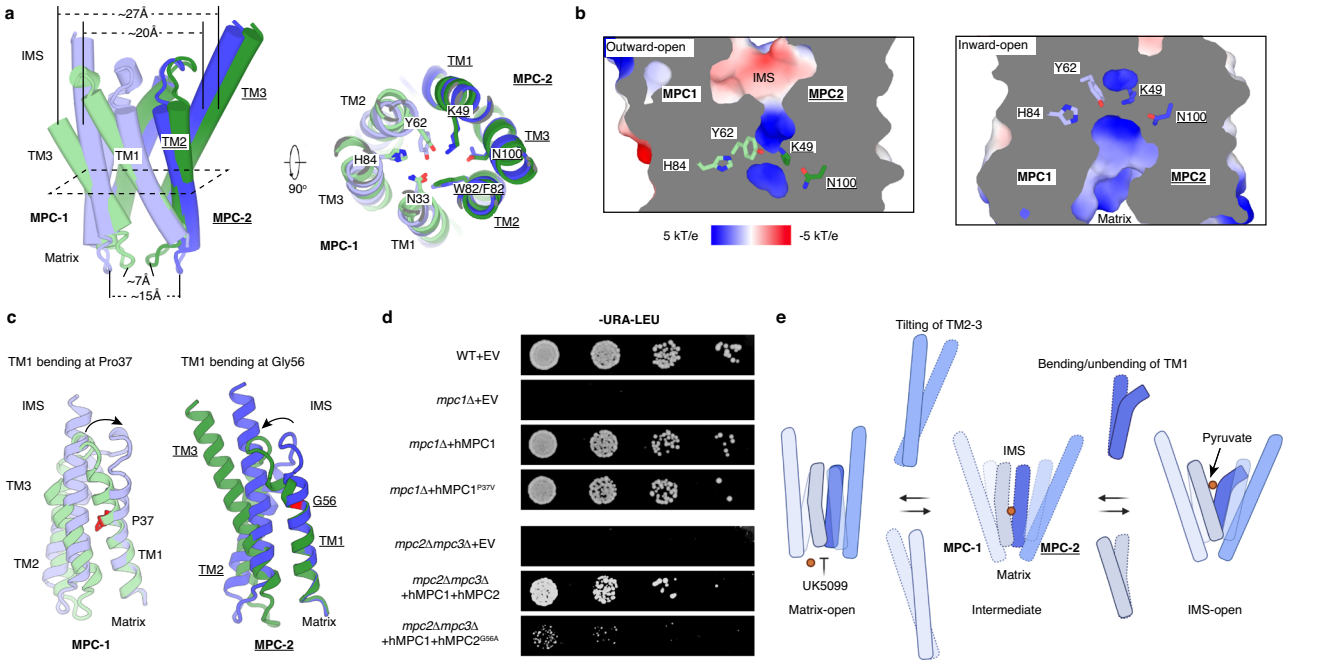

Fig. 5 | Conformational changes of MPC in a pyruvate transport cycle. **a** Structural alignment of MPC1-2 complex in IMS-open and matrix-open states performed using PyMOL, shown as side and top views. The "rotation center" is indicated by a dashed parallelogram in the left panel and the residues located at the rotation center were shown as sticks in the right panel. **b** Electrostatic surface representations of MPC1-2 complex at IMS-open and matrix-open states. The residues located at the rotation center were shown as sticks. **c** Structural comparison of MPC1 and MPC2 at different states. The binding of TM1 at the Pro37 (red) in MPC1 is indicated by an arrow. The binding of TM1 at the Gly56 (red) in MPC2 is indicated by an arrow. **d** Serial dilutions of wild-type (WT), *mpc2*Δ*mpc3*Δ and *mpc1*Δ yeast strains spotted on medium lacking leucine (-URA-LEU). The *mpc1*Δ cells were transformed with wild-type MPC1 or MPC1^{P37V}. The *mpc2*Δ*mpc3*Δ cells were co-transformed with wild-type MPC1 and wild-type MPC2 or MPC2^{G56A}. **e** A working model for pyruvate transport by MPC. Created in BioRender. Qi, X. (2025) https://BioRender.com/todji9n.

while the distance between Ile90 in MPC1-TM3 and Gln74 in MPC2-TM3 decreases from ~15 Å to ~7 Å at the IMS side (Fig. 5a and Supplementary Movie 1).

Despite the significant conformational differences in MPC at both the IMS and matrix sides, the middle portions of the TMs exhibit only limited movement during the transition between the matrix-open and IMS-open states (Fig. 5a). We have designated this region as the "rotation center." This region includes polar residues Asn33, Tyr62, and His84 of MPC1, as well as Lys49, Trp82, and Asn100 of MPC2. These residues are located at the bottom of the inner cavity in the IMS-open conformation and at the top in the matrix-open conformation (Fig. 5b), indicating their potential role in binding pyruvate during conformational transitions. Particularly, Lys49 and Asn100 of MPC2 have been shown to be essential for pyruvate transport (Fig. 3d), in accordance with our structure observations.

To understand the mechanism of conformational changes in MPC, we superimposed the individual MPC1 and MPC2 structures in different states, respectively. The analysis revealed that the TM1 helices of MPC1 and MPC2 undergo distinct conformational changes during the transition (Fig. 5c). At the matrix-open state, TM1 of MPC1 bends at Pro37 toward the center of the MPC1-2 complex, compared to its position in the IMS-open state (Fig. 5c). In contrast, TM1 of MPC2 bends at Gly56 at the IMS-open state, moving away from the center of the complex compared to its position in the matrix-open state (Fig. 5c).

In summary, in the IMS-open state, MPC1-TM1 remains straight while MPC2-TM1 bends outward. Conversely, in the matrix-open state, MPC1-TM1 bends inward while MPC2-TM1 remains straight. No significant conformational changes within the TMs 2-3 of MPC1 and MPC2 were observed between these states (Supplementary Fig. 8e), indicating that MPC undergo asymmetric conformational changes mediated by the bending of TM1 and tilting of TMs 2-3 of both MPC1 and MPC2.

The position of Pro37 in MPC1-TM1 corresponds to the Proline residues in the PQ motifs of TM1 in SemiSWEET (Supplementary Fig. 8f). Previous studies have demonstrated that this Proline residue mediates the conformational transitions of SemiSWEET between outward-open, occluded, and inward-open states[28,29] (Supplementary Fig. 8g). Interestingly, Pro37 is conserved in MPC1 across species but is absent in MPC2, which instead features a Valine residue (Val53) at the corresponding position (Supplementary Fig. 9a–c). However, MPC2-TM1 bends at its top (at Gly56, Fig. 5c), exhibiting a distinct mode of conformational change compared to MPC1 and SemiSWEET.

To elucidate the roles of Pro37 in MPC1-TM1 and Gly56 in MPC2-TM1 during the conformational changes of MPC, we generated the MPC1^{P37V} and MPC2^{G56A} mutants and performed yeast rescue assays. The results revealed that the MPC2^{G56A} mutation impaired the activity of the MPC1-2 complex, whereas the MPC1^{P37V} mutation had no detectable effect (Fig. 5d and Supplementary Fig. 2c, d). These findings indicate that the bending and unbending of MPC2-TM1 is more critical for the asymmetric conformational changes of MPC during pyruvate transport. This mechanism is distinct from that of SemiSWEET, which relies on the bending at a Proline (Pro19 for *Leptospira biflexa* SemiSWEET) in TM1 for its conformational transitions (Supplementary Fig. 8g).

Discussion

MPC and SemiSWEET share the same overall topology and displaying both outward-open (referred to here as matrix-open for MPC) and inward-open (referred to as IMS-open for MPC) conformational states (Figs. 2a, c, 4d and Supplementary Fig. 5c). Therefore, we propose an intermediate or occluded state for MPC based on SemiSWEET structures. In this state, MPC1-TM1 bends inward while MPC2-TM1 remains straight, keeping the IMS gate closed. Simultaneously, TMs 2-3 of both

MPC1 and MPC2 tilt outward, closing the matrix gate, resembling the occluded state of SemiSWEET[28,31,32] (Fig. 5e). This state is unfavorable because the bent MPC1-TM1 does not align with MPC1-TM3, leaving room for conformational dynamics of MPC1-TM1 (Fig. 5e).

Two potential pathways for conformational transitions emerge from this intermediate or occluded state: (1) the top of MPC2-TM1 bends outward to interact with MPC2-TM3, disrupting interactions between MPC1 and MPC2 at the IMS side. Subsequently, MPC1-TM1 unbends and aligns with MPC1-TM3, resulting in the IMS-open conformation (Fig. 5e). (2) MPC1-TM3 tilts inward to align with MPC1-TM1, weakening interactions between MPC1 and MPC2 at the matrix side. This causes the inward tilting of MPC2-TM3 to align with MPC2-TM1, resulting in the matrix-open conformation (Fig. 5e). Interestingly, our cryo-EM map revealed a distinct density located between MPC1-TM1 and MPC2-TM2 in the matrix-open state (Supplementary Fig. 10a, b). This density likely represents an endogenous molecule, as none of the components in the purification buffers could be fitted into it. It may facilitate the interface between the lipid environment and the aqueous chamber. Further investigations are required to identify this molecule and uncover its potential role in MPC regulation.

Remarkably, one polar residue in each TM of MPC1 and MPC2 (Asn33 in TM1, Tyr62 in TM2, and His84 in TM3 of MPC1; Lys49 in TM1, Trp82 in TM2, and Asn100 in TM3 of MPC2) is located at the "rotation center" critical for the tilting of MPC1 and MPC2 during conformational transitions (Fig. 5b). Functional analysis showed that mutants $MPC1^{N33A}$, $MPC1^{Y62F}$, $MPC1^{H84A}$, and $MPC2^{W82F}$ retain activity comparable to wild-type proteins (Figs. 3d and 4a). In contrast, mutations $MPC2^{K49A}$ and $MPC2^{N100A}$ resulted in a near-complete loss of both UK5099 binding and pyruvate transporter activity (Fig. 3c, d). Additionally, a previous study has shown that the thiazolidinedione (TZD) photoprobe could be cross-linked to MPC2 but not MPC1, suggesting that Lys49 and Asn100 of MPC2 may also be essential for TZD binding[41]. Thus, we conclude that MPC2 is primarily responsible for hydrophilic interactions necessary for substrate binding, while both MPC1 and MPC2 contribute to the conformational changes of MPC with different bending patterns. This highlights the unique functional specialization of MPC proteins in the evolutionary development of THB transporters.

Previous studies demonstrated that a ΔpH is required for pyruvate transport by MPC, with pyruvate moving from a region of lower pH to higher pH[21]. Interestingly, Cystinosin is also pH-dependent, and its conformational changes are driven by protons[40]. However, the essential residues for pH sensing in Cystinosin are not conserved in MPC proteins. Additionally, unlike Cystinosin, the conformational states of MPC1-2 complex do not appear to be stabilized by different pH levels (Supplementary Fig. 3a, c, d), and the physiological pH of lysosomes and mitochondria differs significantly. Therefore, it is unlikely that pH affects the pyruvate transport by modulating the conformational changes of MPC. Importantly, our result showed that Lys49 of MPC2 is the most critical polar residue for pyruvate transport, potentially forming hydrophilic interactions with pyruvate (Fig. 3d and Supplementary Fig. 6e). Different pH levels may alter the protonation state of Lys49, leading to a protonated form at lower pH with higher binding affinity for pyruvate and a deprotonated form at higher pH with reduced binding affinity. Further investigations, including structural studies of pyruvate-bound MPC in different states, are needed to fully understand how pH affects pyruvate transport mediated by MPC.

Our structures revealed at least two potential drug-binding sites in MPC. UK5099 binds to the matrix side of MPC, which may represent the binding mode of α-Cyanocinnamate derivatives and TZDs. The pocket within the transmembrane domain opening to the IMS observed in the IMS-open structure could serve as another potential drug-binding which could be targeted for MPC modulation. Our structural insights lay the foundation for identifying endogenous molecules and developing synthetic compounds that modulate MPC activity, which is essential for understanding and treating diseases related to MPC.

Methods

Construct design

The design of $MPC1\text{-}2^{Cryo}$ was adapted from a strategy used for human Spinster 2 (SPNS2) and Vesicular monoamine transporter 2 (VMAT2) structure determination[23,24]. The DARPin protein sequence was fused to various truncations of human MPC2, and the resulting chimeric proteins were subjected to AlphaFold2[25] for structure prediction. The predicted structures were superimposed on both an MBP-DARPin crystal structure (PDB: 1SVX) and a predicted MPC1-2 complex structure, resulting in MPC2-DARPin–MBP–MPC1 complex models. The following criteria were applied for selecting the optimal design: (1) The DARPin fusion should not affect the overall structure of the MPC1-2 complex; (2) The N-terminus of DARPin and the C-terminus of MPC2 should form a stable helix; (3) The MBP should be positioned centrally at the top of the MPC1-2 complex. Based on these criteria, a chimeric MPC2-DARPin protein, with the last three residues of MPC2 deleted, was chosen for expression. MBP was linked to the C-terminus of full-length MPC1 using a 3×GGGGS linker to provide sufficient distance for MBP-DARPin complex formation.

Protein expression and purification

The complementary DNA (cDNA) encoding human MPC1 with a C-terminal Flag tag, MPC2 with a C-terminal 6xHis tag, the designed MPC1-MBP chimeric protein with a C-terminal Strep II tag and the designed MPC2-DARPin chimeric protein with a C-terminal Flag tag were cloned into the pEZT-BM vector, respectively. Mutations were generated by two-step overlapping PCR. The MPC1-2 complex and $MPC1\text{-}2^{Cryo}$ proteins were expressed in HEK293S GnTI$^-$ cells (ATCC) using baculovirus-mediated transduction. Baculoviruses were generated by transfecting Sf9 cells with bacmid encoding the target proteins via Cellfectin II (Gibco). HEK293S GnTI$^-$ cells ($2–3 \times 10^6$ cells/mL, 0.8 L) were infected with 25 mL each of P2 baculoviruses encoding either MPC1 and MPC2, or MPC1-MBP and MPC2-DARPin. Sodium butyrate was added to the cells at a final concentration of 10 mM at 8 h post-infection, and the cells were harvested 48 h post-infection for protein purification.

The cell pellet was resuspended in buffer A (20 mM HEPES pH 7.5, 150 mM NaCl) with 10 μg/mL leupeptin and 1 mM phenylmethylsulfonyl fluoride (PMSF), then disrupted by sonication. The cell lysate was incubated with 1% (w/v) lauryl maltose neopentyl glycol (LMNG, Anatrace) at 4 °C for 1 h. After centrifugation (20,000 g, 4 °C, 30 min) to remove insoluble material, the supernatant was incubated with anti-Flag M2 resin (Sigma) for 1 h at 4 °C. The resin was loaded onto a gravity column, washed with 20 column volumes of buffer B (20 mM HEPES, 150 mM NaCl, 0.01% LMNG, pH 7.5), and the protein was eluted with buffer B containing 0.1 mg/mL 3×Flag peptide. The samples were further purified by size-exclusion chromatography (SEC) on a Superose 6 Increase 10/300 GL column (Cytiva), using buffer B for transporter assays or buffer C (20 mM HEPES pH 7.5, 150 mM NaCl, 0.06% digitonin) for cryo-EM studies. For the $MPC1\text{-}2^{Cryo}$–UK5099 cryo-EM sample, 15 μM UK5099 was added to all purification buffers. Although the binding affinity of UK-5099 to the human MPC1-2 complex was determined to be 88 nM in this study, 15 μM UK-5099 was added to all purification buffers for the $MPC1\text{-}2^{Cryo}$–UK5099 cryo-EM sample to maximize the occupancy of the binding pocket. For $MPC1\text{-}2^{Cryo}$ and $MPC1\text{-}2^{Cryo}$–W82F cryo-EM samples, 500 μM sodium pyruvate was added to all purification buffers.

EM sample preparation and imaging

For grid preparation, each protein sample was concentrated to 12–18 mg/mL with a 100-kDa cutoff concentrator (MilliporeSigma). Then 3 μL of the protein sample was applied to a glow discharged

Quantifoil R1.2/1.3 400 mesh Au holey carbon grid (Quantifoil). The grids were blotted and plunged into liquid ethane using a Vitrobot Mark IV (FEI) and loaded onto a 300 kV Titan Krios transmission electron microscope (FEI) equipped with a Falcon 4i direct electron detector and an energy filter (slit width 10 eV) for data collection. Raw movie stacks were acquired at 0.738 Å per pixel and a nominal defocus range of 0.8–1.8 µm. The dose rate was ~8.5 electrons per pixel per second and the exposure time was 4 s to yield a total dose of ~60 electrons per Å^2 for each movie.

Cryo-EM data processing, structural model building and refinement

For all cryo-EM datasets, motion correction and contrast transfer function (CTF) estimation were performed using cryoSPARC Live[42] with default settings. Low-quality images with ice contaminations were removed, and the remaining images were exported for further processing. For each dataset, approximately 300 images were selected for Blob picking (particle diameter 150–180 Å) in cryoSPARC, and the resulting particles were subjected to 2D classification to generate templates for Template picking (particle diameter 150 Å) across all exported images. Subsequent 2D classifications were performed with default settings. Particles from the top 5–10 classes were selected for ab initio modeling to generate 4 initial models for heterogeneous 3D refinement with default settings. After 2–3 rounds of heterogeneous 3D refinement, the best class was subjected to non-uniform refinement in cryoSPARC with default settings. The subsequent local refinement was performed using the mask generated automatically from the non-uniform refinement (referred to as the global mask in this manuscript) in cryoSPARC with default settings. For the MPC1-2^{Cryo} structure, the cFAR values are moderately low, indicating a preferred orientation of the particles, which may lead to an overestimation of the resolution.

For MPC1-2^{Cryo}–UK5099 and MPC1-2^{Cryo}–W82F, additional local refinements were performed using transmembrane domain weighted masks. For each dataset, densities corresponding to the detergent micelle, MBP, and DARPin were carefully removed from the non-uniform refinement map, leaving only the transmembrane domain of the MPC1-2 complex. This transmembrane-only map was then used to generate a soft mask, which was summed with the global mask to create a hybrid mask. The resulting mask included the micelle, MBP, and DARPin, but applied double weighting to the transmembrane (TM) region. This weighted mask was subsequently used for an additional local refinement to enhance the density quality of the MPC1-2 transmembrane domain.

A composite map for each data set was generated in PHENIX[43] using the cryo-EM maps resulting from the local refinements using the global mask and the transmembrane domain weighted mask. The composite maps were employed for building and refining the MPC1-2 structures. Due to the small size of the transmembrane domain of MPC1-2 and the use of a double-weighted mask, potential artifact cryo-EM densities were observed between the outer ring of the transmembrane domain and the inner ring of the detergent micelle. These artifacts may affect the assignment of side chains that face the outside of the transmembrane domain. In contrast, the residues oriented toward the interior of the transmembrane domain or involved in helix packing show clear densities and were discussed in detail in this manuscript.

The AlphaFold[25] predicted structures of MPC2-DARPin, MPC1, and MBP were docked into the cryo-EM maps as initial models. The coordinates and restraints of UK5099 were generated with eLBOW in PHENIX using the SMILES (Simplified Molecular Input Line Entry System) string from the PubChem database. Manual building and adjustments were performed using COOT[44]. The resulting models were subjected to real-space refinement in PHENIX with default settings including the secondary structure elements, Ramachandran and rotamers restraints. Duo to the low local resolution, residues 1-23, 105-109 of MPC1 and 1-39 of MPC2 were not build in MPC1-2^{Cryo}–UK5099 and residues 1-23, 95-109 of MPC1 and 1-39 of MPC2 were not build in MPC1-2^{Cryo}–W82F structures. The final models were validated in PHENIX, and structural figures were generated using PyMOL (http://www.pymol.org) and ChimeraX[45].

Yeast rescue assay

Yeast strains used in this study are wild-type (S288C): MATa ura3::NatMX; *mpc1*Δ: MATa ura3::NatMX *mpc1*Δ::HYG; *mpc2*Δ*mpc3*Δ: MATa ura3::NatMX *mpc2*Δ::HYG his3::KanMX *mpc3*Δ::ble.

For the assays using *mpc1*Δ strain, the complementary DNA (cDNA) encoding human MPC1, or its mutants was cloned into the pWS158 vector backbone (Addgene # 90517) with a C-terminal Flag tag. For the assays using *mpc2*Δ*mpc3*Δ strain, cDNA encoding human MPC1 with a C-terminal Flag tag and human MPC2 or its mutants with a C-terminal His tag were linked by the "E2A" sequence (GSGATNFSLLKLAGDVELNPGP) and then cloned into the pWS158 vector. The designed MPC1-MBP chimeric protein with a C-terminal Strep II tag and the designed MPC2-DARPin chimeric protein with a C-terminal Flag tag were linked by the same "E2A" sequence and subsequently cloned into the pWS158 vector.

Yeast cultures were grown in 30 °C. Cultures were inoculated the night before in appropriate media and diluted to OD 600 at ~0.2 the next morning and allowed to grow to mid-log phase. For serial dilution growth assays, yeast cells were washed with water and spotted on indicated agar plates in 6-fold dilutions, starting with OD 600 = 0.1. To detect the protein expression in the whole cell lysate, yeast cells were resuspended in 20% trichloroacetic acid (TCA) and incubated on ice for 15 min and washed once in cold acetone. TCA-treated cell pallet was lysed by bead-beating in the lysis buffer (50 mM Tris-HCl pH 7.5, 6 M urea, 1% SDS, 5 mM EDTA, 1 mM DTT, 1 mM PMSF, 10 µM leupeptin, 5 µM pepstatin A, and 1x protease inhibitor cocktail (Roche, 11697498001)). After bead-beating, lysate was incubated in 75 °C for 5 min, centrifuged at 14,000 g for 3 min. Supernatant was collected, normalized by total protein concentration, and used for western blot analysis. The antibodies used for the western blotting were as follows: anti-His (Sigma-Aldrich, 05-949), anti-Flag (MBL Life Science, M185-3L), and anti-Rpn10 (Abcam, ab98843). The images were taken by an Odyssey FC Imager (Dual-Mode Imaging System) and analyzed using Image Studio ver. 5.0 (LI-COR Biosciences, Lincoln, NE). Each experiment was performed at least three times with similar results.

Co-immunoprecipitation

HEK293T cells were set up in 6-well plates and transfected with 0.4 µg human MPC1-Flag plasmids and 0.8 µg human MPC2-His plasmids (or empty vector) using Fugene 6 (Promega) at 60% confluency. Two days post transfection, the cells were harvested in buffer A supplemented with 1% LMNG, 1 mM PMSF and 5 µg/mL leupeptin. The resuspended cells were rotated for 1 h at 4 °C before being centrifuged at 21,000 × *g* for 10 min. The supernatants were then normalized to the same total protein concentration (~4 mg/mL) using lysis buffer. Then 20 µL of the cell lysate was saved as input sample and the rest was mixed with 20 µL of magnetic anti-Flag M2 beads (Sigma) at 4 °C for 1 h. The beads were washed twice with 1 ml buffer B before being eluted with 0.1 mg/ml 3×Flag peptide in buffer B. The antibodies used for the western blotting were as follows: anti-His (Sigma-Aldrich, 05-949), anti-Flag (MBL Life Science, M185-3L), and anti-β-Tubulin (Cell Signaling Technology, 86298). Each experiment was performed at least three times with similar results.

Isothermal titration calorimetry (ITC) analysis

ITC experiments were conducted using a MicroCal ITC200 system (Malvern) at 20 °C in buffer B containing 3% DMSO. A 180 µM solution of UK5099 in the syringe was titrated into ~18 µM of the MPC1-2 complex (wild-type or mutant) through 20 sequential injections of

2-µL aliquots, with a 120-second equilibration period following each injection. The heat released from each injection was integrated, and background heat was subtracted. The data were analyzed using the Wiseman isotherm with the Origin ITC analysis software. Each experiment was repeated at least twice with similar results.

Reporting summary

Further information on research design is available in the Nature Portfolio Reporting Summary linked to this article.

Data availability

The 3D cryo-EM maps have been deposited in the Electron Microscopy Data Bank under the accession numbers EMD-70260 (MPC1-2^{Cryo}), EMD-70348 (MPC1-2^{Cryo}–UK5099, global mask refined), EMD-70349 (MPC1-2^{Cryo}–UK5099, TMs weighted mask refined), EMD-70261 (MPC1-2^{Cryo}–UK5099, composite), EMD-70350 (MPC1-2^{Cryo}–W82F, global mask refined), EMD-70351 (MPC1-2^{Cryo}–W82F, TMs weighted mask refined) and EMD-70262 (MPC1-2^{Cryo}–W82F, composite). Atomic coordinates for the atomic model have been deposited in the Protein Data Bank under the accession numbers 9O9S (MPC1-2^{Cryo}–UK5099) and 9O9T (MPC1-2^{Cryo}–W82F). The raw cryo-EM data for MPC1-2^{Cryo}, MPC1-2^{Cryo}–UK5099, and MPC1-2^{Cryo}–W82F have been deposited in the Electron Microscopy Public Image Archive under accession numbers EMPIAR-12859, EMPIAR-12862, and EMPIAR-12863. Source data are provided with this paper.

References

1. Lunt, S. Y. & Vander Heiden, M. G. Aerobic glycolysis: meeting the metabolic requirements of cell proliferation. *Annu. Rev. Cell Dev. Biol.* **27**, 441–464 (2011).
2. Martinez-Reyes, I. & Chandel, N. S. Mitochondrial TCA cycle metabolites control physiology and disease. *Nat. Commun.* **11**, 102 (2020).
3. Rauckhorst, A. J. & Taylor, E. B. Mitochondrial pyruvate carrier function and cancer metabolism. *Curr. Opin. Genet. Dev.* **38**, 102–109 (2016).
4. Taylor, E. B. Functional properties of the mitochondrial carrier system. *Trends Cell Biol.* **27**, 633–644 (2017).
5. Bender, T., Pena, G. & Martinou, J. C. Regulation of mitochondrial pyruvate uptake by alternative pyruvate carrier complexes. *EMBO J.* **34**, 911–924 (2015).
6. Herzig, S. et al. Identification and functional expression of the mitochondrial pyruvate carrier. *Science* **337**, 93–96 (2012).
7. Bricker, D. K. et al. A mitochondrial pyruvate carrier required for pyruvate uptake in yeast, Drosophila, and humans. *Science* **337**, 96–100 (2012).
8. Tavoulari, S., Sichrovsky, M. & Kunji, E. R. S. Fifty years of the mitochondrial pyruvate carrier: new insights into its structure, function, and inhibition. *Acta Physiol.* **238**, https://doi.org/10.1111/apha.14016 (2023).
9. Vanderperre, B. et al. MPC1-like is a placental mammal-specific mitochondrial pyruvate carrier subunit expressed in postmeiotic male germ cells. *J. Biol. Chem.* **291**, 16448–16461 (2016).
10. Hegazy, L. et al. Identification of novel mitochondrial pyruvate carrier inhibitors by homology modeling and pharmacophore-based virtual screening. *Biomedicines* **10**, https://doi.org/10.3390/biomedicines10020365 (2022).
11. Xu, L., Phelix, C. F. & Chen, L. Y. Structural insights into the human mitochondrial pyruvate carrier complexes. *J. Chem. Inf. Model* **61**, 5614–5625 (2021).
12. Zangari, J., Petrelli, F., Maillot, B. & Martinou, J. C. The multifaceted pyruvate metabolism: role of the mitochondrial pyruvate carrier. *Biomolecules* **10**, https://doi.org/10.3390/biom10071068 (2020).
13. Buchanan, J. L. & Taylor, E. B. Mitochondrial pyruvate carrier function in health and disease across the lifespan. *Biomolecules* **10**, https://doi.org/10.3390/biom10081162 (2020).
14. Sharma, A. et al. Impaired skeletal muscle mitochondrial pyruvate uptake rewires glucose metabolism to drive whole-body leanness. *Elife* **8**. https://doi.org/10.7554/eLife.45873 (2019).
15. McCommis, K. S. et al. Loss of mitochondrial pyruvate carrier 2 in the liver leads to defects in gluconeogenesis and compensation via pyruvate-alanine cycling. *Cell Metab.* **22**, 682–694 (2015).
16. Gray, L. R. et al. Hepatic mitochondrial pyruvate carrier 1 is required for efficient regulation of gluconeogenesis and whole-body glucose homeostasis. *Cell Metab.* **22**, 669–681 (2015).
17. Klemmensen, M. M., Borrowman, S. H., Pearce, C., Pyles, B. & Chandra, B. Mitochondrial dysfunction in neurodegenerative disorders. *Neurotherapeutics* **21**, https://doi.org/10.1016/j.neurot.2023.10.002 (2024).
18. Ghosh, A. et al. Mitochondrial pyruvate carrier regulates autophagy, inflammation, and neurodegeneration in experimental models of Parkinson's disease. *Sci. Transl. Med.* **8**, https://doi.org/10.1126/scitranslmed.aag2210 (2016).
19. Shah, R. C. et al. An evaluation of MSDC-0160, a prototype mTOT modulating insulin sensitizer, in patients with Mild Alzheimer's disease. *Curr. Alzheimer Res.* **11**, 564–573 (2014).
20. Quansah, E. et al. Targeting energy metabolism via the mitochondrial pyruvate carrier as a novel approach to attenuate neurodegeneration. *Mol. Neurodegener.* **13**, https://doi.org/10.1186/s13024-018-0260-x (2018).
21. Tavoulari, S. et al. The yeast mitochondrial pyruvate carrier is a hetero-dimer in its functional state. *EMBO J.* **38**, https://doi.org/10.15252/embj.2018100785 (2019).
22. Binz, H. K. et al. High-affinity binders selected from designed ankyrin repeat protein libraries. *Nat. Biotechnol.* **22**, 575–582 (2004).
23. Chen, H. W. et al. Structural and functional insights into Spns2-mediated transport of sphingosine-1-phosphate. *Cell* **186**, 2644 (2023).
24. Pidathala, S. et al. Mechanisms of neurotransmitter transport and drug inhibition in human VMAT2. *Nature* **623**, 1086–1092 (2023).
25. Jumper, J. et al. Highly accurate protein structure prediction with AlphaFold. *Nature* **596**, 583 (2021).
26. Politte, H., Maram, L. & Elgendy, B. Advances in the development of mitochondrial pyruvate carrier inhibitors for therapeutic applications. *Biomolecules* **15**, https://doi.org/10.3390/biom15020223 (2025).
27. Feng, L. & Frommer, W. B. Evolution of transporters: the relationship of SWEETs, PQ-loop, and PnuC transporters. *Trends Biochem. Sci.* **41**, 118–119 (2016).
28. Latorraca, N. R. et al. Mechanism of substrate translocation in an alternating access transporter. *Cell* **169**, 96 (2017).
29. Lee, Y., Nishizawa, T., Yamashita, K., Ishitani, R. & Nureki, O. Structural basis for the facilitative diffusion mechanism by SemiSWEET transporter. *Nat. Commun.* **6**, https://doi.org/10.1038/ncomms7112 (2015).
30. Feng, L. & Frommer, W. B. Structure and function of SemiSWEET and SWEET sugar transporters. *Trends Biochem. Sci.* **40**, 480–486 (2015).
31. Xu, Y. et al. Structures of bacterial homologues of SWEET transporters in two distinct conformations. *Nature* **515**, 448 (2014).
32. Wang, J. et al. Crystal structure of a bacterial homologue of SWEET transporters. *Cell Res.* **24**, 1486–1489 (2014).
33. Eom, J. S. et al. SWEETs, transporters for intracellular and intercellular sugar translocation. *Curr. Opin. Plant Biol.* **25**, 53–62 (2015).
34. Tao, Y. et al. Structure of a eukaryotic SWEET transporter in a homotrimeric complex. *Nature* **527**, 259–263 (2015).
35. Newstead, S. & Barr, F. Molecular basis for KDEL-mediated retrieval of escaped ER-resident proteins - SWEET talking the COPs. *J. Cell Sci.* **133**, https://doi.org/10.1242/jcs.250100 (2020).
36. Halestrap, A. P. & Denton, R. M. Specific inhibition of pyruvate transport in rat liver mitochondria and human erythrocytes by alpha-cyano-4-hydroxycinnamate. *Biochem. J.* **138**, 313–316 (1974).

37. Halestrap, A. P. The mitochondrial pyruvate carrier. Kinetics and specificity for substrates and inhibitors. *Biochem. J.* **148**, 85–96 (1975).
38. Eberhardt, J., Santos-Martins, D., Tillack, A. F. & Forli, S. AutoDock Vina 1.2.0: new docking methods, expanded force field, and Python bindings. *J. Chem. Inf. Model* **61**, 3891–3898 (2021).
39. Tavoulari, S. et al. Key features of inhibitor binding to the human mitochondrial pyruvate carrier hetero-dimer. *Mol. Metab.* **60**, 101469 (2022).
40. Guo, X. et al. Structure and mechanism of human cystine exporter cystinosin. *Cell* **185**, 3739–3752.e3718 (2022).
41. Colca, J. R. et al. Identification of a mitochondrial target of thiazolidinedione insulin sensitizers (mTOT)-relationship to newly identified mitochondrial pyruvate carrier proteins. *PLoS ONE* **8**, e61551 (2013).
42. Punjani, A., Rubinstein, J. L., Fleet, D. J. & Brubaker, M. A. cryoSPARC: algorithms for rapid unsupervised cryo-EM structure determination. *Nat. Methods* **14**, 290 (2017).
43. Adams, P. D. et al. PHENIX: a comprehensive Python-based system for macromolecular structure solution. *Acta Crystallogr. D* **66**, 213–221 (2010).
44. Emsley, P. & Cowtan, K. Coot: model-building tools for molecular graphics. *Acta Crystallogr. D* **60**, 2126–2132 (2004).
45. Pettersen, E. F. et al. UCSF ChimeraX: structure visualization for researchers, educators, and developers. *Protein Sci.* **30**, 70–82 (2021).

Acknowledgements

We thank X. Li for discussion. Cryo-EM Data were collected at the UT Southwestern Medical Center Cryo-EM Facility (funded in part by the CPRIT Award RP220582). We thank D. Stoddard, J. Martinez-Diaz, C. Baker, R. Welch, L. Esparza and Y. Qin for technical support. Y.S. was a recipient of Postdoctoral Fellowship of American Heart Association (23POST1013018) and D.L. and R.W. were supported by NIH grant (R35GM149533). X.Q. is a CPRIT Scholar and Michael L. Rosenberg Scholar in Medical Research of UT Southwestern Medical Center, and is supported by CPRIT grant (RR230054, to X.Q.) and Welch Foundation (I-2253-20250403, to X.Q.).

Author contributions

X.Q. conceived the project and designed the research with Y.S. and Y.W. Y.W., Y.S., R.W., B.C., A.A. and X.Q. purified the protein. Y.S., Y.W., D.L. and X.Q. carried out cryo-EM work and refined the structures. Y.S., Y.W., Z.X., N.Z. and B.T. contributed to the functional assays. Y.S., Y.W., Z.X. and X.Q. analyzed the data. X.Q. wrote the manuscript.

Competing interests

The authors declare no competing interests.

Additional information

Supplementary information The online version contains supplementary material available at https://doi.org/10.1038/s41467-025-61939-z.

Correspondence and requests for materials should be addressed to Xiaofeng Qi.

Peer review information *Nature Communications* thanks Kyle McCommis, Jens Nielsen and the other, anonymous, reviewer(s) for their contribution to the peer review of this work. A peer review file is available.